



Originally published as:

Alken, P., Maus, S., Lühr, H., Redmon, R. J., Rich, F., Bowman, B., O'Malley, S. M. (2014): Geomagnetic main field modeling with DMSP. - *Journal of Geophysical Research*, 119, 5, p. 4010-4025.

DOI: <http://doi.org/10.1002/2013JA019754>

## RESEARCH ARTICLE

## Geomagnetic main field modeling with DMSP

10.1002/2013JA019754

P. Alken<sup>1</sup>, S. Maus<sup>1</sup>, H. Lühr<sup>2</sup>, R. J. Redmon<sup>1</sup>, F. Rich<sup>3</sup>, B. Bowman<sup>4</sup>, and S. M. O'Malley<sup>5</sup>

## Key Points:

- We calibrated the magnetometers on DMSP F-15 through F-18
- We fit a main field model to the DMSP data
- Our DMSP-based model is validated against Ørsted and ground measurements

## Correspondence to:

P. Alken,  
patrick.alken@noaa.gov

## Citation:

Alken, P., S. Maus, H. Lühr, R. J. Redmon, F. Rich, B. Bowman, and S. M. O'Malley (2014), Geomagnetic main field modeling with DMSP, *J. Geophys. Res. Space Physics*, 119, 4010–4025, doi:10.1002/2013JA019754.

Received 31 DEC 2013

Accepted 22 APR 2014

Accepted article online 29 APR 2014

Published online 27 MAY 2014

<sup>1</sup>National Geophysical Data Center, NOAA, Boulder, Colorado, USA, <sup>2</sup>Helmholtz Centre Potsdam, GFZ, German Research Centre for Geosciences, Potsdam, Germany, <sup>3</sup>Lincoln Laboratory, Massachusetts Institute of Technology, Lexington, Massachusetts, USA, <sup>4</sup>Space Environment Technologies, Pacific Palisades, California, USA, <sup>5</sup>Atmospheric and Environmental Research, Inc., Lexington, Massachusetts, USA

**Abstract** The Defense Meteorological Satellite Program (DMSP) launches and maintains a network of satellites to monitor the meteorological, oceanographic, and solar-terrestrial physics environments. In the past decade, geomagnetic field modelers have focused much attention on magnetic measurements from missions such as CHAMP, Ørsted, and SAC-C. With the completion of the CHAMP mission in 2010, there has been a multiyear gap in satellite-based vector magnetic field measurements available for main field modeling. In this study, we calibrate the special sensor magnetometer instrument on board DMSP to create a data set suitable for main field modeling. These vector field measurements are calibrated to compute instrument timing shifts, scale factors, offsets, and nonorthogonality angles of the fluxgate magnetometer cores. Euler angles are then computed to determine the orientation of the vector magnetometer with respect to a local coordinate system. We fit a degree 15 main field model to the data set and compare with the World Magnetic Model and Ørsted scalar measurements. We call this model DMSP-MAG-1, and its coefficients and software are available for download at <http://geomag.org/models/dmsp.html>. Our results indicate that the DMSP data set will be a valuable source for main field modeling for the years between CHAMP and the recently launched Swarm mission.

## 1. Introduction

Satellite-derived geomagnetic field measurements from recent missions have facilitated the creation of magnetic field models with unprecedented accuracy. These models, in turn, are used in a vast number of different scientific and engineering applications. Low-degree models, such as the World Magnetic Model [Maus *et al.*, 2010a] and the International Geomagnetic Reference Field (IGRF) [Finlay *et al.*, 2010], are used in industry for navigation, orienting antennas and solar panels, and mineral exploration. Scientists subtract these models from geomagnetic data to uncover smaller-scale signatures caused by sources in the Earth's core, crust, and ionosphere. More sophisticated models include a crustal component up to high spherical harmonic degrees, as well as an external field to capture time-varying magnetospheric effects [Sabaka *et al.*, 2004; Maus *et al.*, 2006; Lühr and Maus, 2010; Olsen *et al.*, 2006, 2009; Lesur *et al.*, 2008, 2010]. These models are invaluable in studying the spatial structure and time dependence of the Earth's core, crustal, ionospheric and magnetospheric fields.

While many geomagnetic field models include data recorded by ground observatories, the high accuracy at high spherical harmonic degrees would not be possible without satellite measurements. Many of these models are based on the past decade of measurements by the CHAMP [Reigber *et al.*, 2003], Ørsted [Olsen *et al.*, 2003], and Satélite de Aplicaciones Científicas-C (SAC-C) [Colomb *et al.*, 2004] satellites which have provided unprecedented spatial coverage of the geomagnetic field. Ørsted is the only one of these satellites still in orbit; however, it has provided only scalar field measurements since 2005. Therefore, there have been no scientific-quality vector measurements of the geomagnetic field from satellites since the end of the CHAMP mission in September 2010. While the Swarm satellite mission [Friis-Christensen *et al.*, 2006] was originally scheduled for launch toward the end of CHAMP's mission life, delays have now created a multiyear gap in satellite vector measurements. Filling in this gap would provide a large benefit to studies of secular variation, ionospheric and magnetospheric effects, and main field modeling efforts in the post-CHAMP era.

In this study, we investigate the suitability of the fluxgate magnetometer on board the Defense Meteorological Satellite Program (DMSP) satellites for main field modeling. The primary purpose of the DMSP satellites is for weather specification and nowcasting. Therefore, while they do carry vector magnetometers, the

satellites were not designed to be as magnetically clean as the Ørsted, CHAMP, and Swarm missions. Early DMSP satellites (F-14 and prior) mounted their magnetometers on the body of the satellite leading to significantly higher noise in the magnetic field measurements. Starting with F-15, the magnetometer was mounted on a 5 meter boom assembly which greatly helped reduce the instrument noise and contamination from other spacecraft fields. In our study, we restrict our analysis to the spacecraft F-15 through F-18, which all have boom-mounted magnetometers.

In section 2 we discuss the DMSP fluxgate magnetometer instrument. Section 3 describes the calibration procedure for the vector magnetic measurements, including the timing shift, scalar calibration parameters, and Euler angles. In section 4 we fit a main field model to the calibrated data set. Finally, in section 5 we validate our model against recent Ørsted scalar field measurements and ground observatories.

## 2. DMSP Special Sensor Magnetometer Measurements

The observations used in this study were made by the special sensor magnetometer (SSM) instruments on board the Defense Meteorological Satellite Program (DMSP) satellites F-15, F-16, F-17, and F-18. These DMSP satellites fly in Sun-synchronous, near-polar orbits, with inclinations of about  $98.8^\circ$ , periods of about 102 min, and altitudes between 835 and 850 km [Burke *et al.*, 2011]. F-15 was launched in December 1999 into an orbit with ascending and descending nodes of about 21:10 and 09:10 LT, respectively. F-16 was launched in October 2003 into an orbit with ascending and descending nodes of about 20:01 and 08:01 LT. F-17 was launched in November 2006 with ascending and descending nodes near 17:32 and 05:32 LT. F-18 was launched in October 2009; its ascending and descending nodes are near 19:54 and 07:54 LT.

The SSM instruments are triaxial fluxgate magnetometers mounted on 5 m booms and directed antiradially (upward) from the spacecraft. They measure the geomagnetic field vector at a rate of 12 Hz and with a resolution of 2 nT. These vector measurements are then averaged over 1 s and provided as 1 Hz data in the spacecraft frame. The vector components of the SSM measurements are provided in a coordinate system which we assume to be unknown. We do, however, assume that this system is fixed with respect to the spacecraft, and using our knowledge of the attitude control system, we will define our own spacecraft-fixed coordinate system which will enable us to orient the measurements in a local geocentric frame. This is discussed in detail in the next section.

## 3. Magnetometer Calibration

Some initial calibration of the DMSP SSM data is performed by the Air Force prior to distributing the data publicly. Attempts are made to detect and remove large fields due to the magnetotorquers and instruments on the satellite. Additionally, scalar calibration is performed using the IGRF [Finlay *et al.*, 2010] as the reference field model. However, there continue to exist significant artifacts in the data, including frequent data jumps of 10–30 nT, and systematic large-scale structures which could have adverse effects on accurate main field modeling. Several examples of these effects are shown in Figure 1. Here we plot scalar field intensity residuals from F-17 along a few orbits after subtracting the Pomme-8 main field model [Maus *et al.*, 2010b] for data recorded on 4 May 2011. Pomme-8 is a degree 133 main field model based on CHAMP measurements until 2010 and Ørsted measurements until 2013. It also includes an external field component [Lühr and Maus, 2010]. Specifically, the residual is calculated as

$$r = F_{\text{ssm}} - |\mathbf{B}_{\text{int}} + \mathbf{B}_{\text{ext}}| \quad (1)$$

where  $F_{\text{ssm}}$  is the scalar SSM measurement,  $\mathbf{B}_{\text{int}}$  is the Pomme-8 scalar internal field up to degree 16, and  $\mathbf{B}_{\text{ext}}$  is the Pomme-8 external field. The data jumps in the figure are common features for all DMSP satellites and exist during nearly all orbits we have analyzed. They are likely due to other devices, such as heaters or magnetotorquers, turning on for several minutes and then shutting off, though we have not carefully tracked their origins due to a lack of availability of the satellites' housekeeping data. In addition to the data jumps, we see larger-scale structure, particularly a prominent minimum in the residuals at low latitudes and maxima at higher latitudes. These features could be due to remanent and/or induced magnetization of the spacecraft, insufficiently calibrated data, or differences between Pomme-8 and the main field model used to initially calibrate the data set. Both the small- and large-scale structures seen in the figure could have detrimental effects on attempts to create a main field model, and so it is necessary to carefully detect and

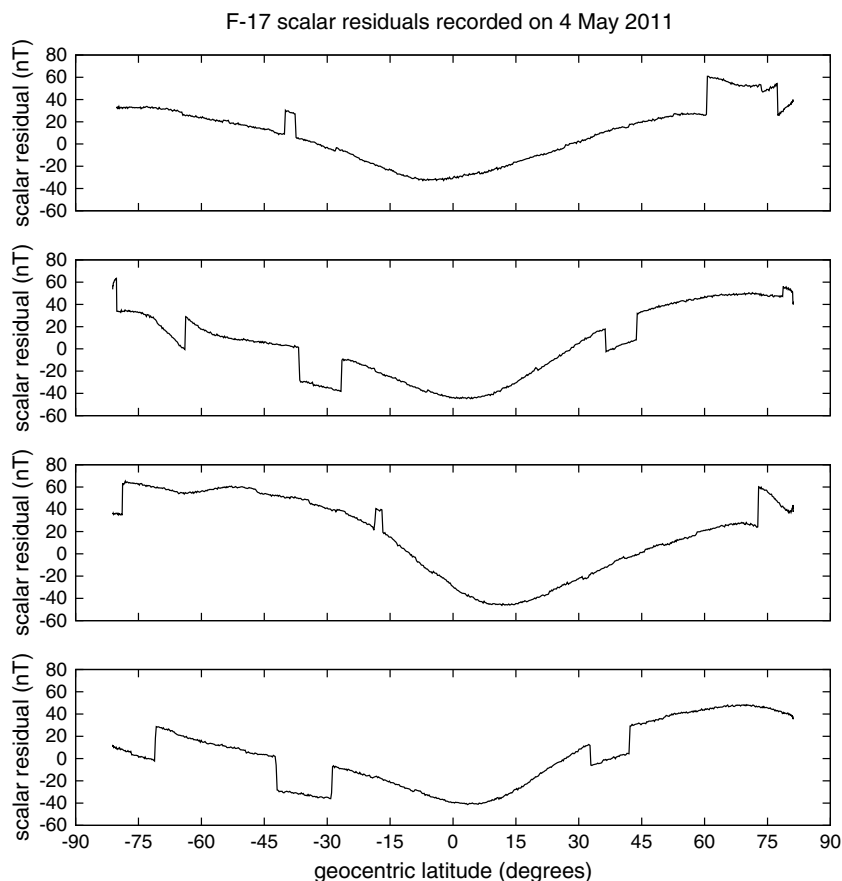


**Figure 1.** Samples of DMSP scalar residuals after subtracting Pomme-8 main field model for several orbital tracks. Data were recorded by F-17 on 4 May 2011.

remove these features from the data. Therefore, we have recalibrated the DMSP SSM measurements using a multistep procedure, following the work performed for other satellite missions [e.g., Yin and Lühr, 2011; Le *et al.*, 2011], which performs both a scalar calibration and a vector calibration to recover the Euler angles required to analyze the data in a geocentric coordinate system.

A key step in calibrating and analyzing the DMSP SSM data lies in accurate orbital position determination. Since the DMSP satellites do not carry GPS receivers, their orbital positions are determined through radar tracking and orbital propagation. The following approach produced orbit ephemerides accurate to within about 30 m. A differential orbit correction program is used to fit Space Surveillance Network (SSN) observations to obtain the standard six Keplerian elements plus the ballistic coefficient ( $B$ ). The Earth gravitational potential model selected for use in the differential orbit corrections is the Earth Gravitational Model 1996 [Lemoine *et al.*, 1998]. The orbital equations also include third-body gravitational effects of the Sun and Moon, solar radiation pressure, Earth and ocean tide effects, and accelerations due to atmospheric drag. The atmospheric density model used in the integration is a modified Jacchia [Jacchia, 1970] 1970 model that was developed for incorporation into the Air Force's High Accuracy Satellite Drag Model (HASDM) program [Storz *et al.*, 2002]. The HASDM model processes drag information from the trajectories of 75 to 80 calibration satellites to solve for a dynamically changing global correction to the thermospheric and exospheric neutral density. For the DMSP satellites the SSN provides a radar track for every pass for every phased-array radar in the network. This provides very accurate radar observations on every single orbit. The orbit accuracy of the DMSP-derived ephemeris has been estimated to have less than a 30 m error at 1 standard deviation throughout the ephemeris.

### 3.1. Coordinate Systems

The DMSP attitude control system is designed to keep the Operational Linescan System instrument aligned with the local geodetic vertical to within  $0.01^\circ$ . This essentially means we can define a satellite-fixed

coordinate system using the local geodetic vertical direction, as well as the satellite's velocity vector. We define unit vectors in our satellite-fixed basis as

$$\hat{s}_1 = \frac{\mathbf{v}_t}{|\mathbf{v}_t|} \quad (2)$$

$$\hat{s}_2 = \hat{s}_3 \times \hat{s}_1 \quad (3)$$

$$\hat{s}_3 = -\hat{e}_\mu \quad (4)$$

where  $\hat{e}_\mu$  is a unit vector in oblate spheroidal coordinates, which is outward normal to the oblate spheroid defined by the World Geodetic System 1984 [National Imagery and Mapping Agency (NIMA), 2000] standard, and  $\mathbf{v}_t = \mathbf{v} - (\mathbf{v} \cdot \hat{e}_\mu)\hat{e}_\mu$  is the component of the satellite velocity perpendicular to  $\hat{e}_\mu$ . With this definition, the basis vector  $\hat{s}_3$  points in the downward local geodetic vertical direction,  $\hat{s}_1$  points along the perpendicular velocity direction, and  $\hat{s}_2$  completes the right-handed basis set. These basis vectors can be assumed to remain fixed with respect to the body of the satellite, up to the error in the attitude control system.

In our analysis, position and velocity vectors are transformed to Earth-centered inertial (ECI) coordinates, which represent standard Cartesian coordinates in a star-fixed frame centered at the Earth's center of mass. ECI coordinates provide a natural basis for solving the orbital equations which produce the DMSP positions and velocities, and they also greatly simplify the various calibration steps described below.

### 3.2. Data Selection

We process all available data from the DMSP F-15, F-16, F-17, and F-18 satellites from January 2009 through July 2013. In order to reduce unmodeled signals from external and ionospheric fields, we impose the following data selection criteria:

1. *Dst* index magnitude does not exceed 30 nT.
2. Interplanetary magnetic field is as follows:  $B_y \leq 2$  nT,  $-2 \leq B_z \leq 6$  nT.
3. *Ap* index is less than 12 at middle/low latitudes ( $\leq 60^\circ$ ).
4. *Ap* index is less than 27 at high latitudes ( $\geq 60^\circ$ ).
5. Local times between 0630 and 1800 are excluded at middle/low latitudes ( $\leq 60^\circ$ ).
6. At high latitudes ( $\geq 60^\circ$ ), the Sun must be at least  $10^\circ$  below the horizon to ensure darkness.

### 3.3. Timing Shift

The first step in calibrating a satellite vector magnetometer is to compute its timing shift. This represents the delay between when a measurement is made by the instrument and when it is given a time stamp and recorded. Due to the various electronics involved, this is typically on the order of several tens of milliseconds, which is significant for satellite measurements as the satellite moves by several hundred meters during this short time. Since the geomagnetic field can change by several nanoteslas over this distance, it is important to accurately account for the timing shift for main field modeling. In order to calculate the timing shift, we calibrate the scalar measurements against the Pomme-8 scalar reference field model. Specifically, we seek a time shift  $\delta t$  which minimizes the error function

$$\epsilon(\delta t) = \sum_i \{F_i - F^{\text{main}}(\mathbf{r}(t_i + \delta t))\}^2 \quad (5)$$

where  $t_i$  is the time stamp recorded with the scalar field measurement  $F_i = |\mathbf{B}_i|$ ,  $F^{\text{main}}$  is the Pomme-8 scalar main field model, and  $\mathbf{r}(t)$  is the satellite position at time  $t$  as given by the orbital propagation procedure discussed previously, and using piecewise cubic Hermite polynomials to interpolate between the sampled points. Hermite polynomials, which fit both orbital positions and velocities, have been shown to exhibit very small errors when interpolating orbit ephemeris with sampling intervals of up to several minutes [Korvenoja and Piche, 2000].

The timing shift  $\delta t$  is calculated from equation (5) using 24 h of data at a time and minimizing the error function using robust regression [Street et al., 1988; Farquharson and Oldenburg, 1998]. Robust regression is used due to the high sensitivity of the timing shift calculation to data outliers as shown in Figure 1. Robust regression is designed to reduce the effect of data outliers by assigning them small weights through iteration. While robust regression helps to counteract the effect of these data jumps, it cannot produce a long-term stable signal of the timing delay on its own, and so we have combined the timing shift calculation with the scalar calibration and outlier detection procedure discussed in the following sections.

### 3.4. Scalar Calibration Parameters

When a timing shift  $\delta t$  has been computed from equation (5), we compute the nine vector magnetometer parameters common to all fluxgate instruments. These are three scale factors, three offsets, and three nonorthogonality angles. The scale factors are typically linear proportionality parameters needed to convert the voltage readings of each magnetometer core into units of magnetic field. However, the DMSP SSM data have already undergone some calibration and is provided in units of magnetic field, and so our scale factors will be dimensionless quantities needed to bring the data into agreement with our scalar reference model. The three offsets represent the magnetic field reading of each magnetometer core if there is no current flowing through the coils. This can be due to remanent magnetization of the core material (or other nearby instruments on the satellite) as well as other sources of noise. Finally, the three nonorthogonality angles allow for the possibility that the three cores are slightly misaligned into a nonorthogonal coordinate system. These angles represent corrections designed to bring the three magnetometer axes into an orthogonal system. The equations relating the calibrated to the uncalibrated field components are discussed in detail in Yin and Lühr [2011] and Lühr *et al.* [2013] and are given below:

$$B_x = S_x E_x + O_x + E_y \cos \alpha_{xy} + E_z \cos \alpha_{xz} \quad (6)$$

$$B_y = S_y E_y + O_y + E_z \cos \alpha_{yz} \quad (7)$$

$$B_z = S_z E_z + O_z \quad (8)$$

These equations represent linearized versions of the relationship. But since the scalar calibration procedure is an iterative process, precise values for the nine magnetometer parameters are obtained after a few cycles. Here  $E_x, E_y, E_z$  represent the uncalibrated SSM field components in the spacecraft frame;  $S_x, S_y, S_z$  are the dimensionless scale factors;  $O_x, O_y, O_z$  are the offsets with units of nanotesla; and  $\alpha_{xy}, \alpha_{xz}, \alpha_{yz}$  are the nonorthogonality angles. The vector  $\mathbf{E}$  is provided by the Air Force in a spacecraft-fixed coordinate system which we are calling  $(x, y, z)$ . Here  $x$  points along the positive spacecraft velocity direction (approximately north/south),  $z$  points normal to the spacecraft and positive toward Earth (approximately downward), and  $y$  points normal to the orbital plane. The precise details of this coordinate system are not too important, since the timing and scalar calibration require only the scalar magnitude of the field vector, and the Euler angles will be computed using our own satellite-fixed basis  $\hat{s}_1, \hat{s}_2, \hat{s}_3$ . The scale factors, offsets, and nonorthogonality angles, however, are referenced to this coordinate system, and so an approximate idea of the axis directions is useful in interpreting their values.

The scale factors, offsets, and nonorthogonality angles are determined by comparing the scalar magnitude of the calibrated vector  $(B_x, B_y, B_z)$  with a known scalar reference model over a period of 24 h of data. Setting  $F_{\text{cal}}^2 = B_x^2 + B_y^2 + B_z^2$ , we can define an error function

$$\epsilon(\mathbf{S}, \mathbf{O}, \alpha) = \sum_i \{F_{\text{cal}}(\mathbf{S}, \mathbf{O}, \alpha; \mathbf{E}_i) - F^{\text{main}}(\mathbf{r}(t_i + \delta t))\}^2 \quad (9)$$

where  $\mathbf{E}_i$  is the SSM vector measurement and  $\delta t$  is the previously computed timing shift. The scale factors, offsets, and nonorthogonality angles are recovered from equation (9) for each 24 h period using nonlinear least squares regression. While only the scalar magnitude of the calibrated field vector is used in the least squares inversion, unique solutions for the scale factors, offsets, and nonorthogonality angles are guaranteed by using 24 h periods of data, representing many orbits over which the magnetometer is rotated into many spatial orientations.

For a research-grade mission such as CHAMP or Oersted, the main field model  $F^{\text{main}}$  would be replaced with an actual scalar field measurement made by a scalar magnetometer located in proximity to the fluxgate instrument. This would provide an independent measurement used to determine the calibration parameters. Since DMSP do not carry scalar magnetometers, the alternative is to use an a priori main field model, such as Pomme-8. Since Pomme-8 is based on CHAMP data until 2010, this choice could introduce errors in to the calibration parameters in the post-CHAMP era. However, in validating the resulting data set against independent observations (see section 5), we believe these errors to be small.

### 3.5. Outlier Detection

As mentioned in section 3.3, data outliers can significantly influence the timing shift calculation, and this is also true for the nine scalar calibration parameters discussed above. During a typical DMSP orbit, there can be between 5 and 10 large data jumps (as seen in Figure 1). It is important to accurately detect and

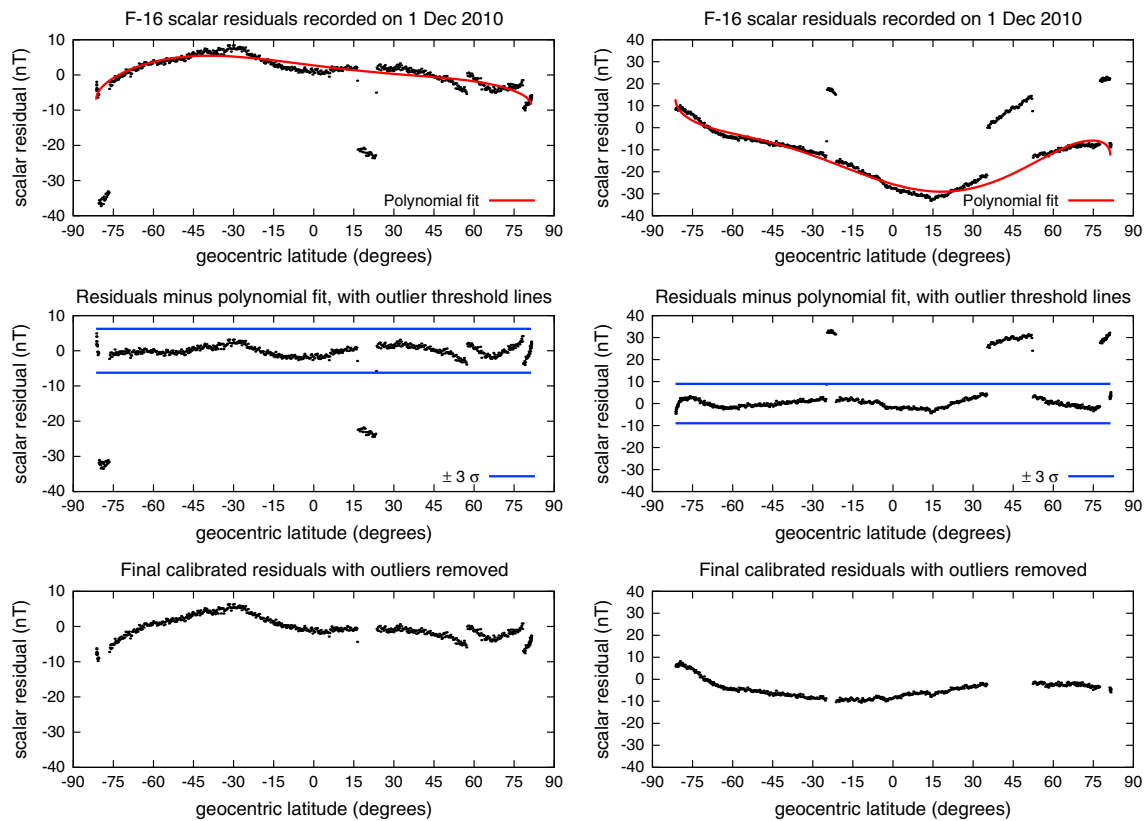


**Figure 2.** Each column contains an example of a magnetic profile with outlier detection iteration. (top) Uncalibrated scalar residual after subtracting Pomme-8 model (black) with robust polynomial fit (red). (middle) Uncalibrated scalar residual minus robust polynomial (black) with  $\pm 3\sigma$  lines (blue) to detect outliers. (bottom) Final residual after applying timing shift and scalar calibration and eliminating outliers. These data were recorded by F-16 during two separate orbits on 1 December 2010.

remove these effects from the data in order to produce reliable long-term signals of the timing shift and scalar calibration parameters.

Detecting these data jumps can be a challenging problem, especially during a first pass of the uncalibrated data where there can be significant structure in the residuals which tends to hide some of the outliers. Therefore, we use an iterative scheme, in which we select a 24 h period of data, calculate a timing shift, calculate the scalar calibration parameters, and then detect and flag outliers in the calibrated data. Flagged outliers are then removed from subsequent iterations. The idea is that during each iteration, the calibrated residuals tend closer and closer to 0, making the data jumps more obvious and easier to detect.

The method we use for outlier detection is to first separate the 24 h period of data into north and south flying half-orbit tracks. For each track, we fit a 5th order polynomial to the scalar residuals as a function of latitude using robust regression to attempt to exclude the outliers. This polynomial is then subtracted from the residuals, and any remaining data point larger than 3 residual standard deviations is considered an outlier and flagged.

The iterative procedure is outlined below:

1. Select a 24 h period of SSM measurements.
2. For iteration  $k$ , compute a timing shift from this data using the procedure discussed in section 3.3, ignoring any flagged outliers.
3. Using the timing shift from the previous step, calculate the nine scalar calibration parameters as outlined in section 3.4.
4. Fit and subtract a degree 5 polynomial in latitude to the calibrated scalar residuals using robust regression and flag any data points larger than 3 standard deviations.
5. Iterate steps 2–4 until no more outliers are detected.

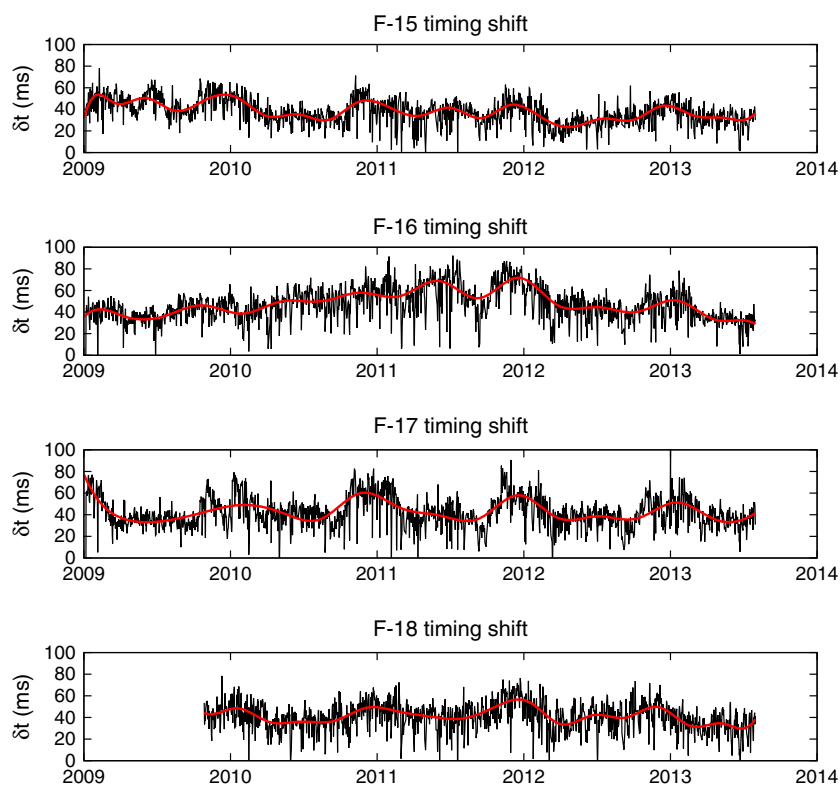


**Figure 3.** Timing shift time series (black) for DMSP satellites from January 2009 through July 2013, except for F-18 which was launched in October 2009. Red curves show smoothing splines used for final timing signal.

This procedure typically converges in about five iterations and works very well for the majority of orbital tracks, but it is not 100% accurate in detecting all data outliers. Problems can arise if there are exceptionally long baseline offsets (lasting many minutes) or if there are jumps near the poles where we select the beginning and end of our orbital tracks. In some of these cases, the polynomial fit to the residuals will be poor which can be detected and used to throw away the entire track. But other cases cannot be so easily detected. However, overall, this procedure works quite well in producing reliable long-term signals of the timing shift and scalar calibration parameters. Figure 2 demonstrates the calibration and outlier iteration procedure discussed above. Each column of the figure contains a single latitudinal profile recorded by F-16 on 1 December 2010. Figure 2 (top) shows the two profiles after subtracting Pomme-8, computing an initial timing shift and scalar calibration and computing a robust polynomial fit to the residuals. Figure 2 (middle) shows the result of subtracting the robust polynomial from the residuals, computing the standard deviation  $\sigma$  of the resulting data and plotting  $\pm 3\sigma$  lines. Data points outside of these lines are flagged as outliers and removed from further processing. The profiles are then iterated several more times until no further outliers are detected. Figure 2 (bottom) shows the final scalar residuals, after removing all outliers and computing and applying final timing shift and scalar calibration parameters. We see that the residual profile in the right column has been significantly flattened over the course of the calibration procedure. This is primarily due to the scalar calibration procedure discussed in section 3.4 and indicates that the original DMSP data were not fully calibrated, leading to minima features at low latitudes.

Figure 3 shows the final timing shift signal for all four satellites. We see significant day-to-day variability, which is likely due to the noise in the data set, and occasionally could result from a failure to detect all outliers as previously discussed. In addition to the day-to-day variability, we see longer-term trends which vary on time scales of a year or more. These are most likely due to thermal noise relating to the amount of sunlight and heat absorbed by the satellite throughout the year. Since these longer-term trends are clearly visible in the signals, we cannot simply use a mean value for the instrument timing. We therefore fit a smoothing spline to the signal for each satellite, shown in red in Figure 3, in order to eliminate the effects of the short-term variability. This smoothing spline is used as the final timing shift.



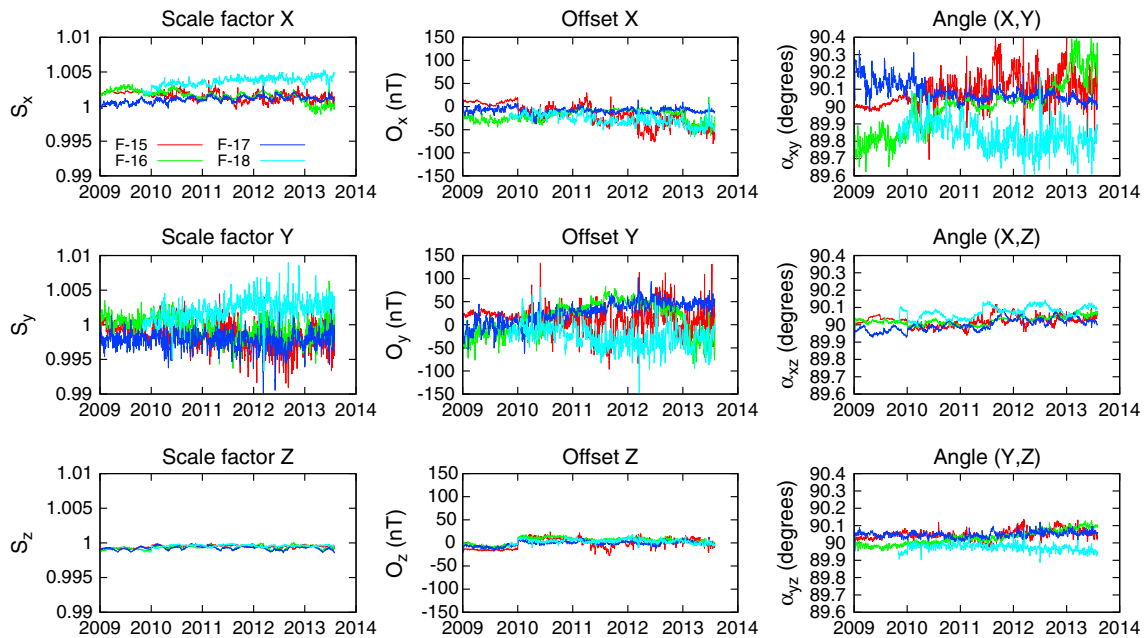


**Figure 4.** Scale factors, offsets, and nonorthogonality angles for F-15 (red), F-16 (green), F-17 (blue), and F-18 (teal). Smoothing splines are fitted to each parameter (not shown).

Figure 4 shows the scalar calibration signals for all four satellites. In the first column we plot the scale factors, which are dimensionless since the DMSP SSM measurements are already provided in units of nanotesla. We see that the X and Z scale factors are relatively low noise and stable over the entire time period. This is because the X and Z directions are roughly equal to the northward and downward directions, respectively, the strongest components of the geomagnetic field, and so are well resolved in the least squares inversion. The Y component on the other hand, which is approximately eastward, represents the weakest component of the geomagnetic field over the orbit and is less well constrained during the inversion. Therefore, we find significant day-to-day noise in this component. The offsets are shown in the middle column and again show relative stability in the X and Z components and higher noise in the Y component. A nice secondary benefit of accurately determining the offsets is the removal of remanent magnetization fields. Since the offsets represent a constant field in the satellite frame, effects of remanent magnetization of materials close to the SSM instrument will be included and thus calibrated out of the data. The nonorthogonality angles are plotted in the last column. Here we see that the angles defined with respect to the poorly resolved Y axis are noisier than  $\alpha_{xz}$ , which measures the angle between the well-resolved X and Z magnetometer axes. In some of the scalar calibration curves we see a significant annual oscillation. We again attribute this to thermal noise related to the amount of sunlight and heat absorbed by the satellite as the Earth orbits the Sun throughout the year. By accurately determining the scalar calibration parameters for each satellite, these thermal effects will be removed from the data set. We fit smoothing splines (not shown) to each scalar calibration parameter similar to the timing signals in order to eliminate the day-to-day noise and keep the longer-term trends in the signals.

### 3.6. Euler Angles

After the timing shift and scalar calibration parameters have been calculated, three Euler angles are computed which rotate the field vector into the spacecraft frame defined by the basis  $\hat{s}_1, \hat{s}_2, \hat{s}_3$ . The DMSP SSM data are already provided in a coordinate system fixed with respect to the satellite (up to errors in the attitude control system), and so we assume a constant three-dimensional rotation from the provided coordinate system to our spacecraft basis. This rotation is defined by three Euler angles  $\alpha, \beta, \gamma$ , and the rotation is given by

$$\mathbf{B}^{\hat{s}}(\alpha, \beta, \gamma) = R_x(\alpha)R_y(\beta)R_z(\gamma)\mathbf{B}^{\text{SSM}} \quad (10)$$

where  $\mathbf{B}^{\text{SSM}}$  is the calibrated magnetic field vector in some arbitrary spacecraft-fixed coordinate system,  $\mathbf{B}^{\hat{s}}$  is the vector in the  $\hat{s}_1, \hat{s}_2, \hat{s}_3$  basis, and the rotation matrices  $R_x, R_y, R_z$  represent rotations around the three

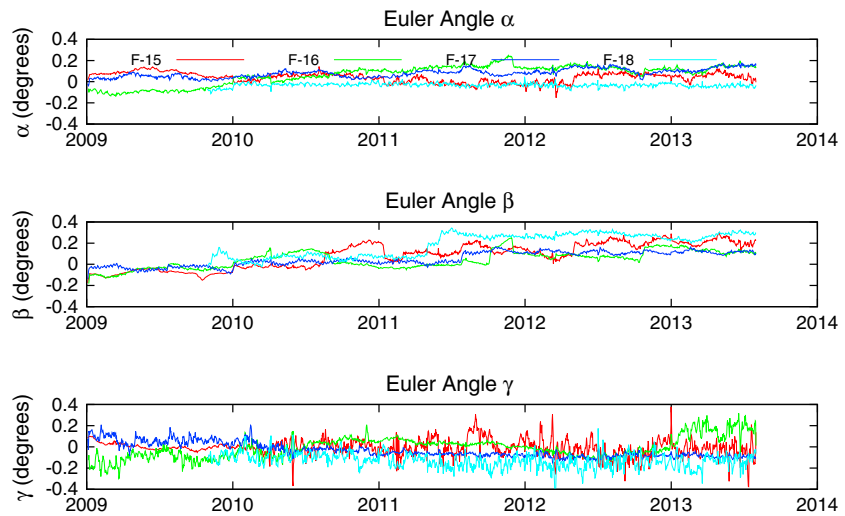


**Figure 5.** Euler angles computed daily for each DMSP satellite. Smoothing splines are fitted to each parameter (not shown).

coordinate axes of the arbitrary spacecraft-fixed system. Once we have the components of the magnetic field in the  $\hat{s}_1, \hat{s}_2, \hat{s}_3$  basis, we may then transform them to geocentric coordinates:

$$\mathbf{B}^{\text{geocentric}}(\alpha, \beta, \gamma) = T\mathbf{B}^{\hat{s}}(\alpha, \beta, \gamma) \quad (11)$$

where the transformation matrix  $T$  is given by

$$T = \begin{pmatrix} \hat{r} \cdot \hat{s}_1 & \hat{r} \cdot \hat{s}_2 & \hat{r} \cdot \hat{s}_3 \\ \hat{\theta} \cdot \hat{s}_1 & \hat{\theta} \cdot \hat{s}_2 & \hat{\theta} \cdot \hat{s}_3 \\ \hat{\phi} \cdot \hat{s}_1 & \hat{\phi} \cdot \hat{s}_2 & \hat{\phi} \cdot \hat{s}_3 \end{pmatrix} \quad (12)$$

and  $\hat{r}, \hat{\theta}, \hat{\phi}$  are the standard geocentric spherical basis vectors and  $\hat{s}_1, \hat{s}_2, \hat{s}_3$  are given in equations (2)–(4). The unknown Euler angles  $\alpha, \beta, \gamma$  are then computed by minimizing the error function

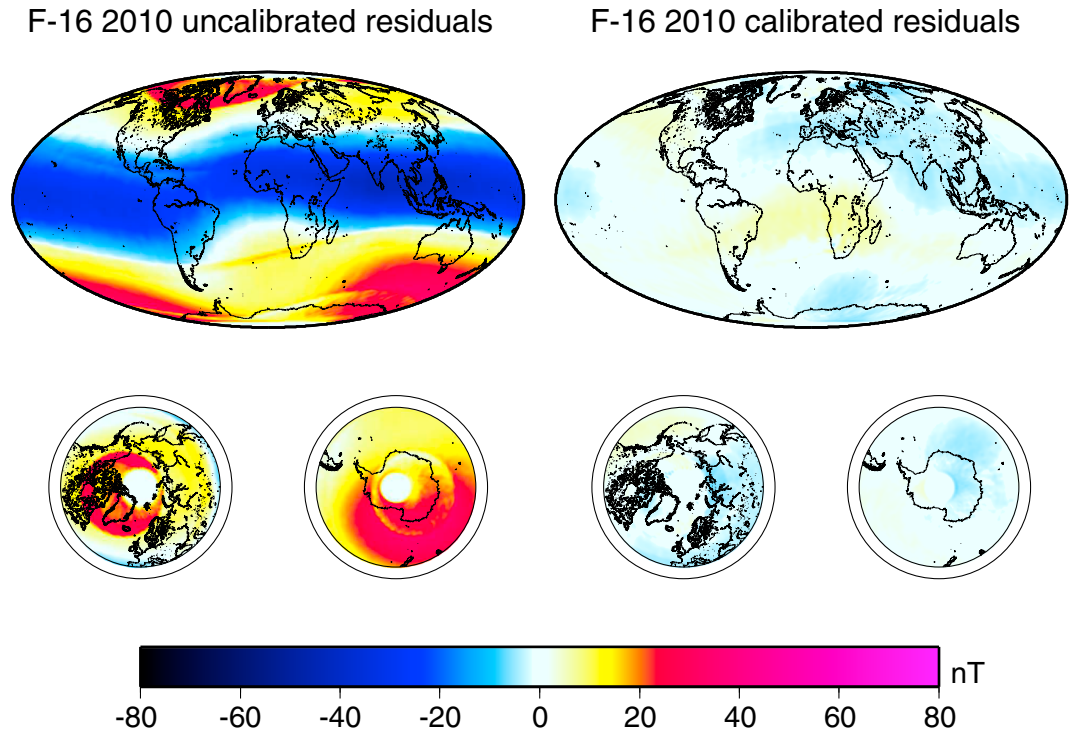
$$\epsilon(\alpha, \beta, \gamma) = \sum_i \left\{ \mathbf{B}_i^{\text{geocentric}}(\alpha, \beta, \gamma) - \mathbf{B}^{\text{main}}(\mathbf{r}(t_i + \delta t)) \right\}^2 \quad (13)$$

where  $\mathbf{B}_i^{\text{geocentric}}$  is the  $i$ th vector measurement are computed for each 24 h time period, and time series of  $\alpha, \beta, \gamma$  are shown in Figure 5 for each of the DMSP satellites.

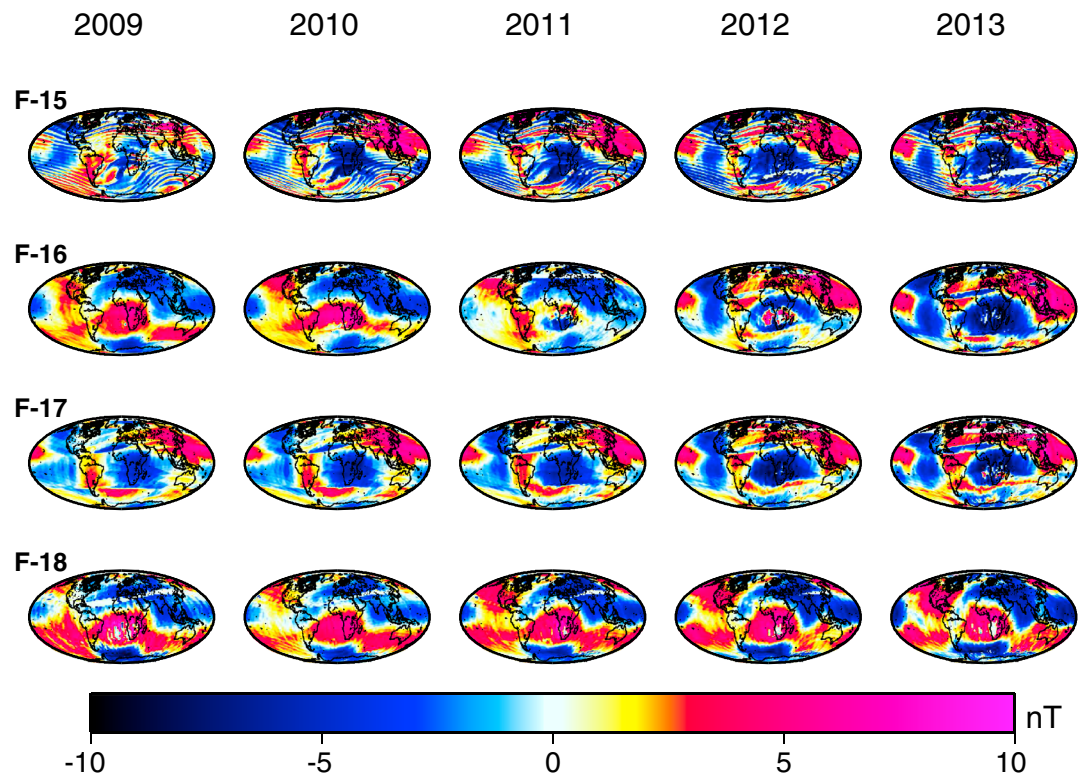
### 3.7. Final Calibrated Residuals

Figure 6 shows the scalar residuals for F-16 taking all data for 2010, binning it in latitude and longitude and averaging each bin. We select 2010 since that was the last year of CHAMP vector measurements, and so the Pomme-8 model is more accurate during that time frame. Figure 6 (left) shows the original, uncalibrated data after subtracting Pomme-8. We see here the distinctive band of minima at low latitudes, seen earlier in Figure 1. The residuals are on the order of 80 nT, which is far too large for accurate main field modeling. In Figure 6 (right) we show the same data set after performing the timing, scalar, and Euler angle calibration, and eliminating outliers. Here we plot the data set on the same 80 nT scale, but the residuals are in fact closer to 10 nT. Additionally, the systematic structure at low latitudes has largely disappeared as a result of the calibration.

Figure 7 shows the calibrated scalar residuals for all satellites F-15 through F-18 for the years 2009–2013, plotted on a scale of 10 nT. For each year, the data are binned in latitude and longitude and averaged over the year. Figure 8 shows the downward component calibrated  $B_z$  residuals for the same years. These are on the order of 30 nT for 2009–2011 and get larger in the later years 2012–2013. This is because the Pomme-8 model used to calibrate the data set is primarily based on CHAMP measurements and therefore cannot accurately predict the secular variation after 2010.



**Figure 6.** Pomme-8 scalar residuals for F-16 averaged over 2010 gridded in latitude and longitude (left) prior to calibration and (right) after calibration.



**Figure 7.** Calibrated scalar residuals for all satellites F-15 through F-18 and years 2009–2013.

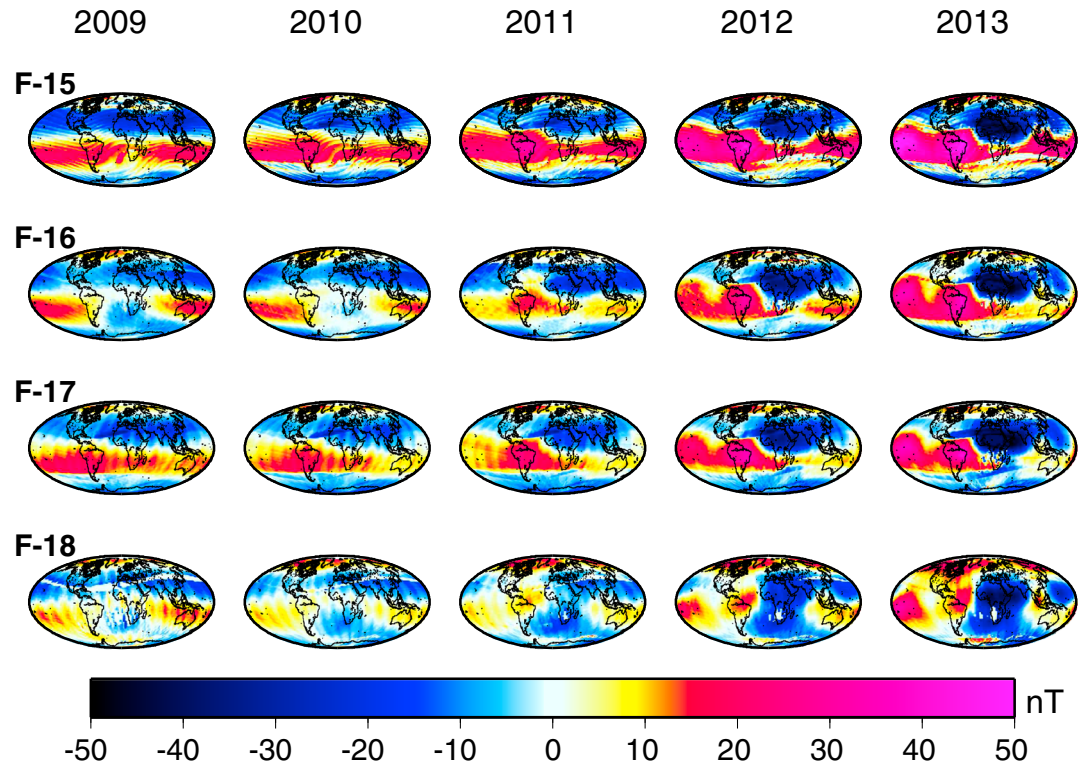


Figure 8. Calibrated  $B_z$  residuals for all satellites F-15 through F-18 and years 2009–2013.

#### 4. Main Field Modeling

Next we fit a spherical harmonic degree 15 main field model to the calibrated DMSP data set. The model is given by

$$B_x = \sum_{nm} \left(\frac{a}{r}\right)^{n+2} (g_{nm}(t) \cos m\phi + h_{nm}(t) \sin m\phi) \frac{\partial}{\partial \theta} P_{nm}(\cos \theta) \quad (14)$$

$$B_y = \frac{1}{\sin \theta} \sum_{nm} \left(\frac{a}{r}\right)^{n+2} m (g_{nm}(t) \sin m\phi - h_{nm}(t) \cos m\phi) P_{nm}(\cos \theta) \quad (15)$$

$$B_z = - \sum_{nm} (n+1) \left(\frac{a}{r}\right)^{n+2} (g_{nm}(t) \cos m\phi + h_{nm}(t) \sin m\phi) P_{nm}(\cos \theta) \quad (16)$$

where the degree  $n$  is summed from 1 to 15, order  $m$  is summed from 0 to  $n$ ,  $r, \theta, \phi$  are the standard geocentric spherical coordinates,  $P_{nm}(\cos \theta)$  is the Schmidt seminormalized associated Legendre function,  $a$  is the geomagnetic reference radius (6371.2 km), and the time-dependent coefficients are given by

$$g_{nm}(t) = g_{nm}^0 + \dot{g}_{nm}(t - t_0) + \frac{1}{2} \ddot{g}_{nm}(t - t_0)^2 \quad (17)$$

$$h_{nm}(t) = h_{nm}^0 + \dot{h}_{nm}(t - t_0) + \frac{1}{2} \ddot{h}_{nm}(t - t_0)^2 \quad (18)$$

with the main field coefficients  $g_{nm}^0, h_{nm}^0$ , secular variation coefficients  $\dot{g}_{nm}, \dot{h}_{nm}$ , and secular acceleration coefficients  $\ddot{g}_{nm}, \ddot{h}_{nm}$  to be determined. The epoch  $t_0$  was chosen as 2012.0. The unknown coefficients are computed through robust regression using all calibrated DMSP data from 2010.5 through 2013.5. A 3 year period was chosen since the model's time dependence is represented by a quadratic polynomial, and 3 years of data were found to be long enough to accurately determine the secular acceleration. Only the vertical  $B_z$  component and scalar magnitude of the DMSP data were used for the modeling, since the  $B_x$  and  $B_y$  components are highly influenced by ionospheric and magnetospheric currents at high latitudes. The  $B_z$  component is also influenced to a lesser extent by these systems; however, it is required to include this in the modeling since the scalar data alone cannot guarantee a unique solution [Backus, 1986]. Therefore, we

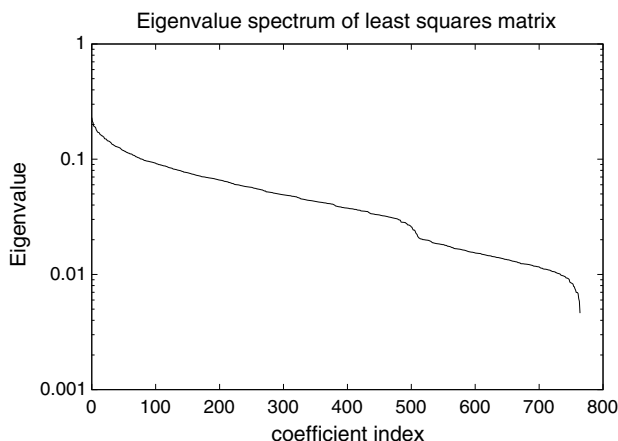


**Figure 9.** Eigenvalue spectrum of model least squares matrix as a function of coefficient index.

sampled regions with larger areas (typically low latitudes) and downweight densely sampled regions with smaller areas (typically at the poles).  $K$  is a normalization constant chosen so that  $\sum_{ij} w_{ij} = 1$ . Applying these weights to the data significantly reduces the condition number of the least squares matrix and improves the resulting solution.

Further reduction of the matrix condition number was achieved by nondimensionalizing the time-dependent factors  $t - t_0$  in the model and applying Tikhonov regularization [Tikhonov et al., 1995] to the secular variation and secular acceleration coefficients above degree 8. Damping these coefficients helps to mitigate the effect of the polar data gap due to DMSP’s inclination of 98.8°. The nondimensionalization was achieved by defining a new variable  $\tilde{t}_i = (t_i - t_0 - \mu_t) / \sigma_t$ , where  $\mu_t$  and  $\sigma_t$  are the mean and standard deviation of all  $t_i - t_0$  values used in the inversion. In equations (17) and (18),  $\tilde{t}$  was then used in place of  $t - t_0$ . The final  $g_{nm}$  and  $h_{nm}$  are then rescaled back to physical units. Additional weighting factors are computed via iteratively reweighted least squares using the Huber weighting function [Huber, 1996]. At each

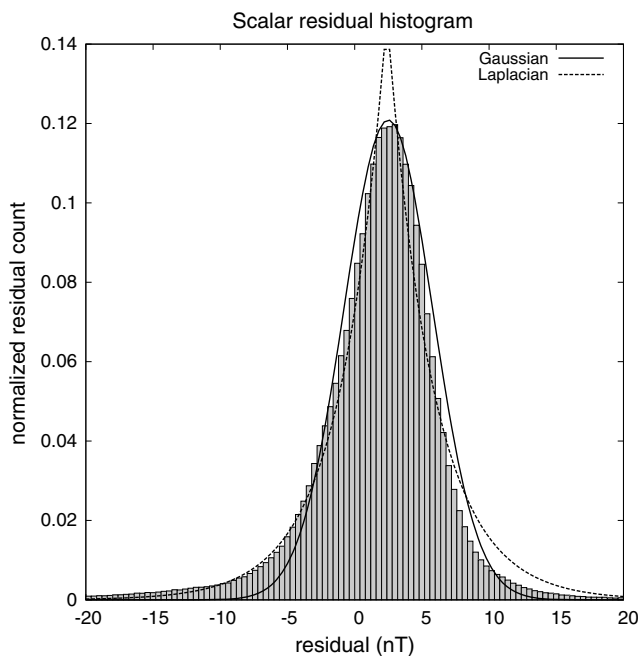


**Figure 10.** Residual histograms for the internal field. (top) Histogram of scalar residuals. (bottom) Histogram of  $B_z$  residuals. Histograms are normalized by the total count of the data.

use the  $B_z$  component data only below 55° latitude to minimize the influence of high-latitude currents and use the scalar data at all latitudes.

Since the polar regions are sampled much more frequently than middle and low latitudes, we organize the data into 1.8° latitude by 3.6° longitude bins and assign initial weights to the data as

$$w_{ij} = \frac{1}{K} \sqrt{\frac{a_{ij}}{n_{ij}}} \quad (19)$$

where  $a_{ij}$ ,  $n_{ij}$  are the area on a unit sphere and number of measurements for bin  $(i, j)$ , respectively. These are designed to upweight sparsely

sampled regions with larger areas (typically low latitudes) and downweight densely sampled regions with smaller areas (typically at the poles).  $K$  is a normalization constant chosen so that  $\sum_{ij} w_{ij} = 1$ . Applying these weights to the data significantly reduces the condition number of the least squares matrix and improves the resulting solution. Further reduction of the matrix condition number was achieved by nondimensionalizing the time-dependent factors  $t - t_0$  in the model and applying Tikhonov regularization [Tikhonov et al., 1995] to the secular variation and secular acceleration coefficients above degree 8. Damping these coefficients helps to mitigate the effect of the polar data gap due to DMSP’s inclination of 98.8°. The nondimensionalization was achieved by defining a new variable  $\tilde{t}_i = (t_i - t_0 - \mu_t) / \sigma_t$ , where  $\mu_t$  and  $\sigma_t$  are the mean and standard deviation of all  $t_i - t_0$  values used in the inversion. In equations (17) and (18),  $\tilde{t}$  was then used in place of  $t - t_0$ . The final  $g_{nm}$  and  $h_{nm}$  are then rescaled back to physical units. Additional weighting factors are computed via iteratively reweighted least squares using the Huber weighting function [Huber, 1996]. At each step of the iteration, these Huber weights are multiplied by the initial weights in equation (19) to produce the final weights. This procedure helps to minimize the effect of data outliers on the final model. The system is iterated 5 times to achieve convergence. The condition number of the final least squares matrix was 49.6, and the corresponding eigenvalue spectrum is shown in Figure 9. We see here that the spectrum decreases relatively smoothly with coefficient index, indicating that the secular variation and acceleration coefficients are well constrained in the model. The residual histograms for the scalar and  $B_z$  data are shown in Figure 10. There is a bias of about 3 nT in the scalar residuals and about 1 nT in the  $B_z$  residuals. The bias arises primarily due to errors in the Pomme-8 external field, which is subtracted from the data prior to fitting the internal field model. If the external field

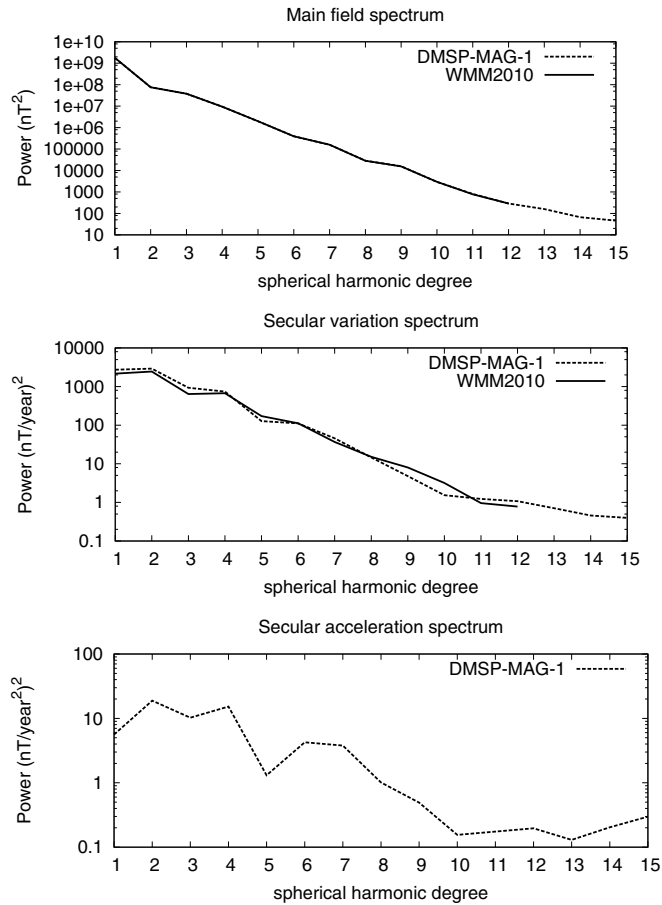


**Figure 11.** Main field, secular variation, and secular acceleration coefficients of DMSP-MAG-1 compared with WMM2010 (WMM2010 does not provide secular acceleration).

model underestimates the true external field, this would lead to the nonzero residual means shown in the figure. The expected residual distribution for Huber weighting is Gaussian for small residuals and Laplacian for the larger residuals in the tail. These curves are plotted on top of the histogram and show that the smaller residuals indeed agree well with a Gaussian distribution. While the larger negative residuals agree fairly well with the Laplacian curve, the large positive residuals exhibit differences due to an asymmetry in the residuals. This asymmetry could be due to errors in the external field model or various sources of noise in the data set. We call the resulting model DMSP-MAG-1, and its coefficients and software are available on the web at <http://geomag.org/models/dmsp.html>.

**4.1. External Field**

We include a simple model of fields originating in the magnetosphere and their induced counterparts. Here we allow for an external field aligned with the dipole component of the main field, in addition to the steady ring current. The field can be represented as

$$\mathbf{B}_{\text{ext}} = \text{RC} + E_{st} \sum_{m=0}^1 \begin{bmatrix} (\tilde{g}_{1m} \cos m\phi + \tilde{h}_{1m} \sin m\phi) \partial_{\theta} P_{1m} \\ \frac{m}{\sin \theta} (\tilde{g}_{1m} \sin m\phi - \tilde{h}_{1m} \cos m\phi) P_{1m} \\ (\tilde{g}_{1m} \cos m\phi + \tilde{h}_{1m} \sin m\phi) P_{1m} \end{bmatrix} + I_{st} \left(\frac{a}{r}\right)^3 \sum_{m=0}^1 \begin{bmatrix} (\tilde{g}_{1m} \cos m\phi + \tilde{h}_{1m} \sin m\phi) \partial_{\theta} P_{1m} \\ \frac{m}{\sin \theta} (\tilde{g}_{1m} \sin m\phi - \tilde{h}_{1m} \cos m\phi) P_{1m} \\ -2(\tilde{g}_{1m} \cos m\phi + \tilde{h}_{1m} \sin m\phi) P_{1m} \end{bmatrix} \quad (20)$$

where  $(\tilde{g}_{10}, \tilde{g}_{11}, \tilde{h}_{11}) = \frac{1}{\sqrt{g_{10}^2 + g_{11}^2 + h_{11}^2}} (g_{10}, g_{11}, h_{11})$  are the normalized main field dipole coefficients computed previously,  $E_{st}$  and  $I_{st}$  are the external and induced components of the external dipole field aligned with the main field [Maus and Weidelt, 2004], and RC represents the steady ring current field. The term RC is also a degree 1 spherical harmonic expansion of the external field, whose coefficients we took from Pomme-8. The above external field model offers a first-order approximation to the true external field, since a more sophisticated model would separate the contributions of the inner and outer magnetosphere into solar

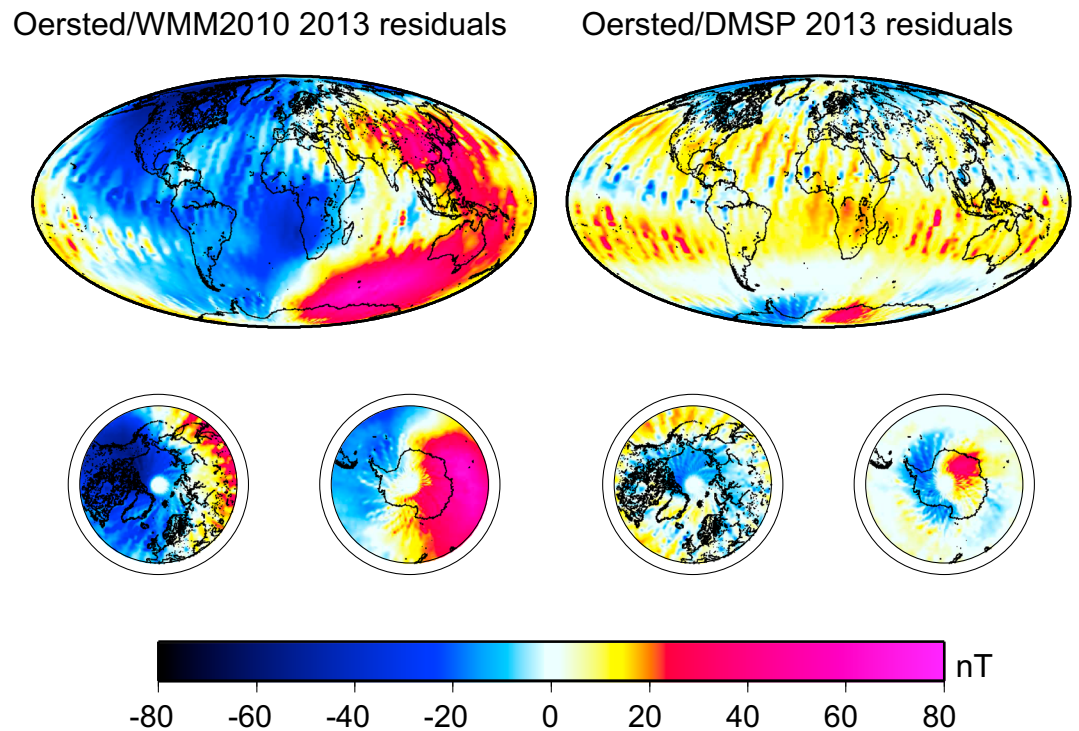


**Figure 12.** Residuals of Ørsted scalar data with (left) WMM2010 and (right) DMSM-MAG-1 from January through June 2013.

magnetic and geocentric solar magnetospheric coordinates [Maus and Lühr, 2005; Lühr and Maus, 2010]. In a future study, we will investigate the construction of a more realistic external field model from the DMSM data set.

### 5. Validation

We perform several validations of the model DMSM-MAG-1. The first is to compare with the World Magnetic Model (WMM) 2010 [Maus et al., 2010a]. WMM2010 is a degree 12 main field model based on data from CHAMP, Ørsted, and ground magnetic observatories prior to and including 2010. In order to make a realistic comparison, we recalculated a DMSM-based model using data from 2009 to 2011 and using the same epoch  $t_0 = 2010.0$  as the WMM2010. Figure 11 shows the main field and secular variation spectra for the two models, as well as the secular acceleration of DMSM-MAG-1. The main field coefficients agree very well while the secular variation exhibits small differences above spherical harmonic degree 9. This could be due to the polar data gap in the DMSM data set.

Next, we compare DMSM-MAG-1 with recent Ørsted satellite scalar data. We selected all available Ørsted data from January to June 2013 using the same data selection criteria discussed in section 3.2. Then we constructed a model based on the DMSM satellites from January 2010 through July 2013. The residuals were binned in latitude and longitude and averaged and are shown in Figure 12 (right). For comparison, we also show the Ørsted residuals against WMM2010 in Figure 12 (left). We can see that the DMSM residuals are significantly smaller than the WMM2010 for 2013. The RMS difference over the globe is 11.4 nT for DMSM and 20.8 nT for WMM2010.

Another validation was done by comparing the model secular variation with observations at three ground observatories. Data from the International Real-time Magnetic Observatory Network (INTERMAGNET) observatories Kourou (KOU, 5.21°N, 307.27°E), Mbour (MBO, 14.38°N, 343.03°E), and Tamanrasset (TAM, 22.79°N, 5.53°E) was processed to compute monthly mean differences and compute secular variations in the X, Y, and Z components from 2010 to mid-2013. These signals are shown in blue in Figure 13. Then, a series of models were fitted to the calibrated DMSM data set, using sliding 3 year window of data centered on the model epoch  $t_0$ , and advancing the window by 30 days to produce secular variation models for a set of

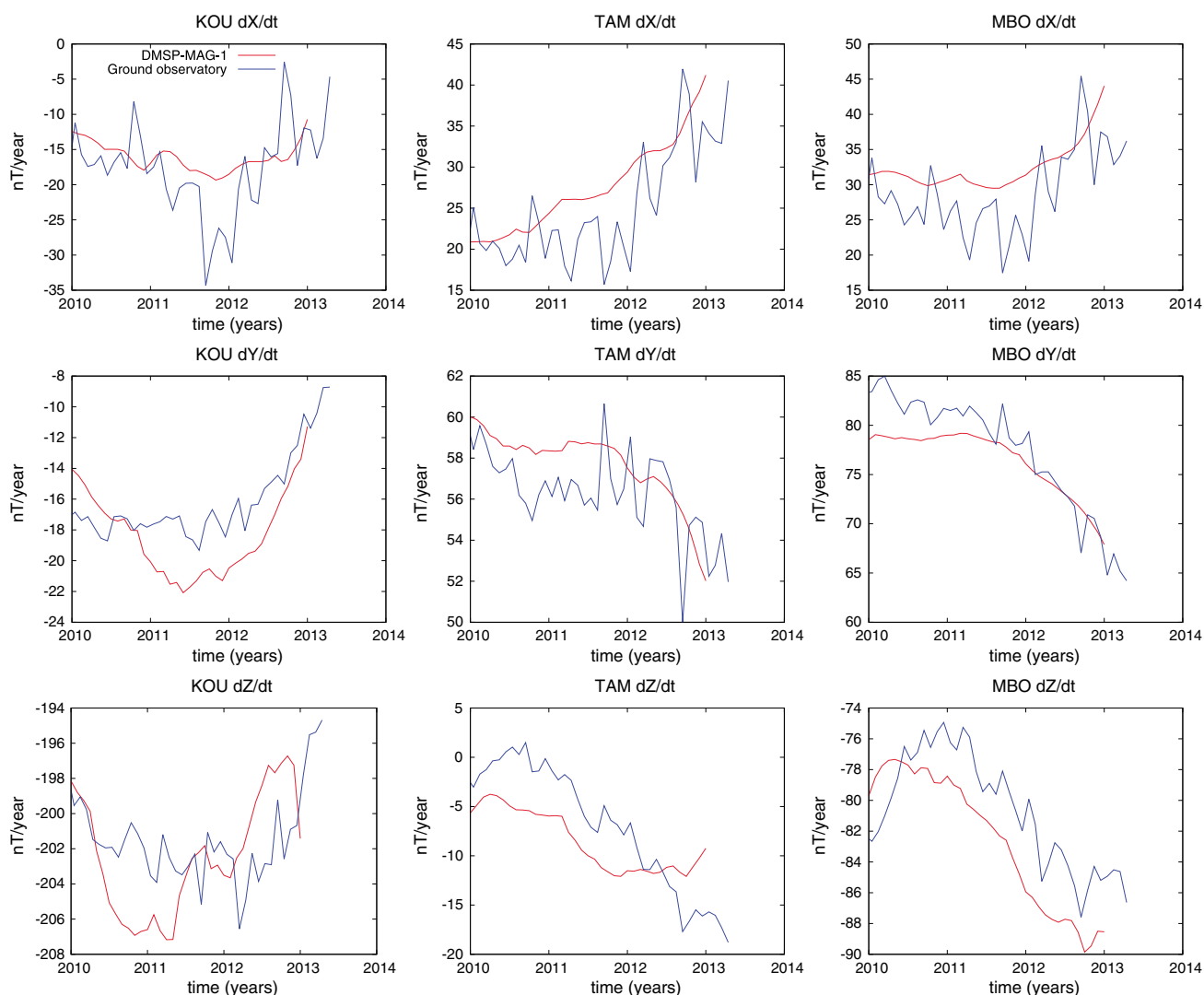


**Figure 13.** Secular variation in X, Y, Z observed at (left) KOU, (middle) TAM, and (right) MBO in blue. Corresponding predictions from DMSP-MAG-1 shown in red.

epochs during the same time period. These curves are shown in red in the figure. The observatory data exhibit significant monthly variations, due mainly to external field contributions which are not modeled in the internal field secular variation of the DMSP-based models. The three observatories are located in regions which have very different secular variation magnitudes, but the DMSP-based models are able to reproduce the correct magnitude and general trend of the observatory data. The RMS difference between the observatory data and model is about 5.1 nT in the X component, 2.1 nT in Y, and 3.8 nT in Z.

## 6. Conclusion

We have calibrated the vector fluxgate magnetometer instruments on the DMSP F-15, F-16, F-17, and F-18 satellites to obtain a data set suitable for main field modeling in the post-CHAMP era. First, careful orbit determination was performed to yield ephemeris accurate to within 30 m at 1 standard deviation over the orbit. Next, we calculated the instruments' timing shifts, scalar calibration parameters, and Euler angles, in addition to carefully detecting and removing outliers due to other spacecraft fields. The resulting calibrated data set, when compared with Pomme-8, has RMS scalar residuals of about 10 nT and RMS  $B_z$  residuals of about 30 nT. We fit a degree 15 main field model to the calibrated DMSP data set and find good agreement with WMM2010 during the years 2009–2011. When compared with recent Ørsted scalar measurements, our DMSP-MAG-1 model offers a significant improvement over WMM2010, yielding RMS differences of about 11 nT, compared with 21 nT for WMM2010. Furthermore, DMSP-MAG-1 is able to accurately predict observed



secular variation during the 2010–2013 period at the three INTERMAGNET observatories studied. We believe that this data set will offer a valuable source of vector geomagnetic measurements in the years between CHAMP and the Swarm mission.

### Acknowledgments

The DMSP magnetometer data are publicly available from the NOAA National Geophysical Data Center (NGDC) through arrangement with the Air Force Research Laboratory (AFRL) and the Defense Meteorological Satellite Program (DMSP). The CHAMP mission was sponsored by the Space Agency of the German Aerospace Center (DLR) through funds of the Federal Ministry of Economics and Technology. The Ørsted Project was made possible by extensive support from the Ministry of Trade and Industry, the Ministry of Research and Information Technology, and the Ministry of Transport in Denmark.

Larry Kepko thanks the reviewers for their assistance in evaluating this paper.

### References

- Backus, G. (1986), Poloidal and toroidal fields in geomagnetic field modeling, *Rev. Geophys.*, *24*(1), 75–109.
- Burke, W. J., G. R. Wilson, C. S. Lin, F. J. Rich, J. O. Wise, and M. P. Hagan (2011), Estimating *Dst* indices and exospheric temperatures from equatorial magnetic fields measured by DMSP satellites, *J. Geophys. Res.*, *116*, A01205, doi:10.1029/2010JA015310.
- Colomb, F. R., C. Alonso, C. Hofmann, and I. Nollmann (2004), SAC-C mission, an example of international cooperation, *Adv. Space Res.*, *34*(10), 2194–2199, doi:10.1016/j.asr.2003.10.039.
- Farquharson, C. G., and D. W. Oldenburg (1998), Non-linear inversion using general measures of data misfit and model structure, *Geophys. J. Int.*, *134*, 213–227, doi:10.1046/j.1365-246x.1998.00555.x.
- Finlay, C. C., et al. (2010), International geomagnetic reference field: The eleventh generation, *Geophys. J. Int.*, *183*(3), 1216–1230, doi:10.1111/j.1365-246X.2010.04804.x.
- Friis-Christensen, E., H. Lühr, and G. Hulot (2006), Swarm: A constellation to study the Earth's magnetic field, *Earth Planets Space*, *58*, 351–358.
- Huber, P. J. (1996), *Robust Statistical Procedures*, CBMS-NSF Regional Conference Series in Applied Mathematics, Society for Industrial and Applied Mathematics, Philadelphia, Pa.
- Jacchia, L. G. (1970), New static models of the thermosphere and exosphere with empirical temperature profiles. *SAO Special Report, Smithsonian Astrophys. Obs. Special Report*, 313.
- Korvenoja, P., and R. Piche (2000), Efficient satellite orbit approximation, in *Proceedings of the 13th International Technical Meeting of the Satellite Division of the Institute of Navigation (ION GPS 2000)*, pp. 1930–1937, Institute of Navigation (ION), Salt Lake City, Utah.
- Le, G., W. J. Burke, R. F. Pfaff, H. T. Freudenreich, S. Maus, and H. Lühr (2011), C/NIFS measurements of magnetic perturbations in the low-latitude ionosphere during magnetic storms, *J. Geophys. Res.*, *116*, A12230, doi:10.1029/2011JA017026.
- Lemoine, F. G., et al. (1998), The development of the joint NASA GSFC and NIMA geopotential model EGM96, Goddard Space Flight Center, Greenbelt. *NASA/TP-1998-206861*, Goddard Space Flight Center, Greenbelt, Md.
- Lesur, V., I. Wardinski, M. Rother, and M. Manda (2008), GRIMM: The GFZ Reference Internal Magnetic Model based on vector satellite and observatory data, *Geophys. J. Int.*, *173*, 382–394, doi:10.1111/j.1365-246X.2008.03724.x.
- Lesur, V., I. Wardinski, S. Asari, B. Minchev, and M. Manda (2010), Modelling the Earth's core magnetic field under flow constraints, *Earth Planets Space*, *62*(6), 503–516, doi:10.5047/eps.2010.02.010.
- Lühr, H., and S. Maus (2010), Solar cycle dependence of quiet-time magnetospheric currents and a model of their near-Earth magnetic fields, *Earth Planets Space*, *62*, 843–848.
- Lühr, H., F. Yin, and R. Bock (2013), Magnetic properties of CHAMP and their effects on in-orbit calibration, *J. Sens. Sens. Syst.*, *2*, 9–17, doi:10.5194/jsss-2-9-2013.
- Maus, S., and H. Lühr (2005), Signature of the quiet-time magnetospheric magnetic field and its electromagnetic induction in the rotating Earth, *Geophys. J. Int.*, *162*, 755–763, doi:10.1111/j.1365-246X.2005.02691.x.
- Maus, S., and P. Weidelt (2004), Separating the magnetospheric disturbance magnetic field into external and transient internal contributions using a 1D conductivity model of the Earth, *Geophys. Res. Lett.*, *31*, L12614, doi:10.1029/2004GL020232.
- Maus, S., M. Rother, C. Stolle, W. Mai, S. Choi, H. Lühr, D. Cooke, and C. Roth (2006), Third generation of the Potsdam Magnetic Model of the Earth (POMME), *Geochem. Geophys. Geosyst.*, *7*, Q07008, doi:10.1029/2006GC001269.
- Maus, S., S. Macmillan, S. McLean, B. Hamilton, A. Thomson, M. Nair, and C. Rollins (2010a), The US/UK World Magnetic Model for 2010–2015. *NOAA Tech. Rep. NESDIS/NGDC*, British Geological Survey.
- Maus, S., C. Manoj, J. Rauberg, I. Michaelis, and H. Lühr (2010b), NOAA/NGDC candidate models for the 11th generation International Geomagnetic Reference Field and the concurrent release of the 6th generation Pomme magnetic model, *Earth Planets Space*, *62*, 729–735.
- National Imagery and Mapping Agency (NIMA) (2000), Department of Defense World Geodetic System 1984, its definition and relationships with local geodetic systems, *Tech. Rep. TR8350.2*, National Imagery and Mapping Agency, St. Louis, MO, U.S.A.
- Olsen, N., H. Lühr, T. J. Sabaka, M. Manda, M. Rother, L. Tøffner-Clausen, and S. Choi (2006), CHAOS—A model of the Earth's magnetic field derived from CHAMP, Ørsted, and SAC-C magnetic satellite data, *Geophys. J. Int.*, *166*(1), 7–75, doi:10.1111/j.1365-246X.2006.02959.x.
- Olsen, N., M. Manda, T. J. Sabaka, and L. Tøffner-Clausen (2009), CHAOS-2—A geomagnetic field model derived from one decade of continuous satellite data, *Geophys. J. Int.*, *179*(3), 1477–1487, doi:10.1111/j.1365-246X.2009.04386.x.
- Olsen, N., et al. (2003), Calibration of the Ørsted vector magnetometer, *Earth Planets Space*, *55*, 11–18.
- Reigber, C., H. Lühr, and P. Schwintzer (2003), *First CHAMP Mission Results for Gravity, Magnetic and Atmospheric Studies*, Springer, Berlin Heidelberg.
- Sabaka, T. J., N. Olsen, and M. E. Purucker (2004), Extending comprehensive models of the Earth's magnetic field with Ørsted and CHAMP data, *Geophys. J. Int.*, *159*, 521–547, doi:10.1111/j.1365-246X.2004.02421.x.
- Storz, M., B. R. Bowman, and J. I. Branson (2002), High Accuracy Satellite Drag Model (HASDM), *AIAA-2002-4886*, AIAA/AAS Astrodynamics Specialist Conference and Exhibit 5-8 August 2002, Monterey, Calif.
- Street, J. O., R. J. Carroll, and D. Ruppert (1988), A note on computing robust regression estimates via iteratively reweighted least squares, *Am. Stat.*, *42*, 152–154.
- Tikhonov, A., A. Goncharkov, V. Stepanov, and A. G. Yagola (1995), *Numerical Methods for the Solution of Ill-Posed Problems, Mathematics and Its Applications*, Springer, Berlin, Germany.
- Yin, F., and H. Lühr (2011), Recalibration of the CHAMP satellite magnetic field measurements, *Meas. Sci. Technol.*, *22*(5), 055101, doi:10.1088/0957-0233/22/5/055101.